

Article

Machine Learning-Based Prediction of Stability in High-Entropy Nitride Ceramics

Tianyu Lin ¹, Ruolan Wang ² and Dazhi Liu ^{3,*}¹ School of Design, Kookmin University, Souel 02707, Republic of Korea; lintianyu210@naver.com² China Institute for Visual Studies, China Academy of Art, Hangzhou 310000, China; ruolan1020@foxmail.com³ Xiamen Academy of Arts and Design, Fuzhou University, Fuzhou 350000, China

* Correspondence: liudazhi19770809@163.com

Abstract: The field of materials science has experienced a transformative shift with the emergence of high-entropy materials (HEMs), which possess a unique combination of properties that traditional single-phase materials lack. Among these, high-entropy nitrides (HENs) stand out for their exceptional mechanical strength, thermal stability, and resistance to extreme environments, making them highly sought after for applications in aerospace, defense, and energy sectors. Central to the design of these materials is their entropy forming ability (EFA), a measure of a material's propensity to form a single-phase, disordered structure. This study introduces the application of the sure independence screening and sparsifying operator (SISSO), a machine learning technique, to predict the EFA of HEN ceramics. By utilizing a rich dataset curated from theoretical computational data, SISSO has been trained to identify the most critical features contributing to EFA. The model's strong interpretability allows for the extraction of complex mathematical expressions, providing deep insights into the material's composition and its impact on EFA. The predictive performance of the SISSO model is meticulously validated against theoretical benchmarks and compared with other machine learning methodologies, demonstrating its superior accuracy and reliability. This research not only contributes to the growing body of knowledge on HEMs but also paves the way for the efficient discovery and development of new HEN materials with tailored properties for advanced technological applications.

Keywords: high-entropy materials; high-entropy nitride ceramics; entropy forming ability; machine learning; sure independence screening and sparsifying operator; material stability



Citation: Lin, T.; Wang, R.; Liu, D. Machine Learning-Based Prediction of Stability in High-Entropy Nitride Ceramics. *Crystals* **2024**, *14*, 429. <https://doi.org/10.3390/cryst14050429>

Academic Editor: Francisco M. Morales

Received: 2 April 2024
Revised: 28 April 2024
Accepted: 29 April 2024
Published: 30 April 2024



Copyright: © 2024 by the authors. Licensee MDPI, Basel, Switzerland. This article is an open access article distributed under the terms and conditions of the Creative Commons Attribution (CC BY) license (<https://creativecommons.org/licenses/by/4.0/>).

1. Introduction

The emergence of HEMs has marked a paradigm shift in materials science, introducing a novel class of materials with a unique combination of properties that are not typically found in traditional single-phase materials [1–6]. These materials, characterized by the presence of four or more principal elements in equiatomic or near-equiatomic ratios, have been shown to exhibit exceptional mechanical strength, thermal stability, and resistance to extreme environments [7–9]. HENs, in particular, have garnered significant interest due to their potential for high-temperature applications and their ability to withstand harsh conditions, such as radiation and corrosive environments [10,11]. Moskovskikh et al. introduced a significant advancement in the fabrication of bulk HENs, achieving exceptional mechanical properties with hardness up to 33 GPa and fracture toughness up to 5.2 MPa·m^{1/2} [12]. The design and development of HENs are crucial to advancing technologies in aerospace, defense, and energy sectors, where materials with superior performance are in high demand. Comparing high-entropy alloys (HEAs) with HENs, HEAs typically form single-phase solid solutions due to high entropy, while nitrogen introduction in HENs may encourage diverse phase development, including nitride phases. To harness the full potential of HENs, enhancing their stability becomes imperative. A critical concept in the rational design of HEAs is the EFA [13], which serves as a measure of

the material's ability to form a single-phase, disordered structure. The EFA is intrinsically linked to the configurational entropy of a material, which is a key factor in stabilizing the single-phase structure and enhancing the material's overall performance [14]. A high EFA value indicates a lower energy penalty for the formation of a disordered phase, suggesting a greater likelihood of achieving a stable, homogeneous material. This descriptor has become an essential tool for predicting the formation of single-phase HEMs and has been instrumental in guiding the search for new materials with desired properties and performance characteristics [15–17].

The traditional approach to discovering and characterizing new materials has been largely empirical and iterative, involving extensive experimental trials and characterizations. Computational methods, such as first-principles calculations and phase diagram analyses, have been crucial in predicting the material's various properties [18–20], thereby accelerating the development of new materials. However, these traditional computational techniques can be computationally intensive and time-consuming, particularly for the vast compositional space of HEMs when calculating the EFA. With the advent of machine learning (ML) techniques, the field of materials science has witnessed a significant shift towards a more data-driven and predictive approach [21–23]. ML algorithms have been successfully applied to model complex relationships between material compositions, structures, and properties, enabling the rapid identification of promising materials and the optimization of their properties [24]. In the context of HEMs, ML has been particularly impactful, with studies demonstrating the ability to predict phase stability, mechanical properties, and other critical characteristics with high accuracy [25–27].

Building on the transformative impact of ML in the realm of HEMs, it is important to note that the versatility of ML extends beyond the domain of high-entropy ceramics. For instance, Schlenz et al. [28] have recently employed machine learning to identify suitable chemical compositions for new perovskite-type oxygen transport membranes, highlighting the power of data-driven methods in materials science. In the specific context of HEMs, Kaufmann et al. [17] and Zhang et al. [16] have pioneeringly applied ML techniques to predict the properties of high-entropy carbide ceramics, showcasing the potential of data-driven methods in accelerating the discovery of new HEMs. While their work has emphasized the importance of integrating chemical descriptors and thermodynamic features into ML models for accurate predictions of phase stability and material properties, there is room to enhance the interpretability of these models. The ability to understand the relationships between material composition and predicted properties is crucial for the rational design of new materials.

Inspired by this, in this study, we aim to further advance the application of ML in the field of HEMs by employing the SISO [29] method to predict the EFA of HEN ceramics. Recognized as a “white-box model,” SISO offers strong interpretability, enabling it to output complex mathematical expressions similar to symbolic regression [30]. This feature highlights the impact of each feature or descriptor on the prediction, providing insights into the material's essence and facilitating the rapid design and synthesis of new materials, such as the discovery of new perovskite tolerance factors to predict whether ABO_3 type compounds possess the perovskite structure [31]. SISO's expertise lies in extracting the most critical features and their combinations from a massive feature space, which is crucial for regression and classification tasks in data mining. This method is particularly adept at handling large and correlated feature spaces, a common challenge in the intricate compositional landscape of HEMs. By harnessing SISO's capabilities, we aimed to develop a predictive model that not only identified materials with high EFA values but also shed light on the factors contributing to the formation and stability of single-phase HENs, thereby enhancing our understanding of these complex materials.

Our research adopted a data-driven approach by constructing a SISO model, which was informed by an extensive dataset of HENs [32]. The performance of our SISO model was meticulously validated against theoretical benchmarks documented in the literature and benchmarked against existing ML methodologies. This rigorous evaluation

demonstrated the SISO model's proficiency in predicting the EFA of HENs, underscoring its effectiveness as a predictive tool. Besides leveraging the "white-box" nature of our chosen machine learning method, we provide interpretable mathematical expressions that offer deep insights into the material's composition and its impact on EFA, which is a novel contribution to the understanding of HENs. Through this research, we aimed to contribute to the burgeoning understanding of HEMs and their diverse applications. Our predictive model is envisioned to become an invaluable asset for materials researchers, enhancing the efficiency of discovering new HEN materials with tailored properties, potentially accelerating the innovation cycle in materials science.

2. Materials and Methods

2.1. Data Collection and Integration

The accuracy and robustness of our predictive models hinge on a well-curated dataset that captures the complexity and diversity of HEN ceramics. The compounds in this dataset contained eight elements: Al, Ti, V, Cr, Zr, Nb, Mo, and Si. The dataset was strategic and grounded in the existing literature on HENs. These elements were chosen for their diverse physical and chemical properties, including varying electronegativity, atomic size, and crystal structure preferences, which are known to significantly influence the formation and properties of nitrides. The propensity of these elements is to form rock-salt structure B1 nitrides with nitrogen (except for Si) [33,34]. Si was specifically included due to its unique role in forming single-phase HEN ceramics when combined with other elements, adding an extra layer of complexity and potential for novel material discovery [35]. Overall, these selections are particularly relevant as they encompass elements that are among the most commonly and successfully used to create high-entropy ceramics with improved mechanical properties, thermal stability, and resistance to extreme environments.

For the initial prediction phase, we compiled a dataset of 56 samples, each with its corresponding EFA value as the target property. These EFA values were sourced from the theoretical computational data based on bulk HEN ceramic materials featuring face-centered cubic structures [32]. The EFA values are shown in Table A1. In the subsequent prediction phase, we expanded our compositional scope by introducing Hf, Ta, and W into the mix with the previously selected elements, resulting in 210 novel HEN ceramics. The EFA values for these HEN ceramics had not been previously calculated by DFT. We utilized the trained model to rapidly compute the EFA values for these 210 novel HEN ceramics without the need for DFT calculations and identify compounds with high EFA values.

The EFA equation in our study is as follows [32]:

$$H_{mix} = \frac{\sum_{i=1}^n g_i H_i}{\sum_{i=1}^n g_i} \quad (1)$$

$$EFA = \left[\sqrt{\frac{\sum_{i=1}^n g_i (H_i - H_{mix})^2}{(\sum_{i=1}^n g_i) - 1}} \right]^{-1} \quad (2)$$

where n denotes the overall count of distinct geometric configurations that were sampled, with g_i referring to the degeneracy and H_i representing formation enthalpy associated with each configuration. Consequently, H_{mix} is estimated by calculating the average of the formation enthalpy across the whole distinct supercell configurations.

To obtain a comprehensive set of features for each composition, we employed the Magpie [36], which utilizes a high-throughput approach to generate a rich set of descriptors based on the basic chemical and physical properties of the constituent elements. These descriptors include atomic radii, electronegativities, ionization energies, and crystal structure preferences, among others, providing a multifaceted view of the elemental combinations and their potential impact on the material properties. The 124-dimensional feature vectors obtained from Magpie were subjected to a rigorous preprocessing regimen to ensure the quality and relevance of the data for the SISO analysis. This process involved the

imputation of any missing values, ensuring that the dataset was complete and consistent. Specifically, we integrated the use of matminer's IonProperty module [37] to estimate some missing ionic properties, such as the mean ionic character, which were not directly available from the Magpie-generated dataset. This step was crucial to the comprehensive analysis of the material's composition and its impact on EFA. Additionally, we performed feature selection to remove any redundant or irrelevant variables that could potentially skew the analysis or reduce the model's predictive power. This careful curation of the feature space was essential for the success of the SISSO method in identifying the most relevant descriptors and building accurate predictive models.

The final, preprocessed dataset was then integrated with the EFA target values to form the complete dataset used for both the training and prediction phases of our study. This integrated dataset served as the backbone of our analysis, allowing us to probe the intricate relationships between the elemental composition and the resulting EFA, ultimately leading to the discovery of new HEN ceramics with promising characteristics.

2.2. Machine Learning

In this study, we employed SISSO, a compressed-sensing-based dimensionality reduction method, to identify the optimal low-dimensional descriptors for the materials science data. The SISSO method, as detailed in Ouyang et al. [29], is designed to tackle immense and potentially correlated feature spaces. A key advantage of SISSO is its ability to distill a complex, high-dimensional dataset into a smaller set of descriptors that are not only relevant but also interpretable. By leveraging domain knowledge or intuition, SISSO can propose a select few key features that capture the essence of the data, leading to models with strong interpretability. This feature-based approach ensures that the resulting solutions are not only accurate but also provide insights into the underlying mechanisms and relationships within the materials science data, converging to the best solution by meticulously selecting a relevant subset of features from a vast array of candidates.

2.2.1. Feature Space Construction

The cornerstone of the SISSO method is the construction of an extensive feature space, Φ_0 , which is initiated with a set of primary features that are hypothesized to capture the essential characteristics of the material property under investigation. These primary features encompass a range of atomic-scale properties. The method of obtaining these features in this work is detailed in Section 2.1. The feature space was then expanded through the recursive application of a comprehensive set of algebraic and functional operations, including addition, subtraction, multiplication, division, exponentiation, and logarithms, etc. This recursive process generated a rich set of derived features, which were hypothesized to capture the complex relationships between the atomic-scale properties and the macroscopic material behavior. In this work, we applied

$$\Theta = (+, -, \times, \div, \exp, \ln) \quad (3)$$

to Φ_0 two times to generate the descriptor spaces Φ_1 and Φ_2 . If applied too many times, the formula is prone to overfitting [38].

2.2.2. Sure Independence Screening (SIS)

The SISSO algorithm leverages sure independence screening (SIS) to effectively reduce the dimensionality of the feature space. SIS scores each feature based on its correlation with the target property, retaining only the top-ranked features that exhibit the strongest relationship with the property of interest. This step is crucial in managing the computational complexity of the subsequent analysis, because it filters out the less informative features and focuses on those that are most likely to contribute to the predictive model.

2.2.3. Sparsifying Operator (SO)

Following the dimensionality reduction via SIS, the sparsifying operator (SO) was employed to identify the optimal descriptor from the selected subset of features. The SO operates by solving an underdetermined system of linear equations, seeking a sparse solution that minimizes the reconstruction error while maintaining sparsity. This approach ensures that the final descriptor is not only accurate but also computationally efficient, as it avoids overfitting by retaining only the most significant features.

2.2.4. Model Building and Validation

The SISSO method iteratively explores higher-dimensional solutions, incrementally adding features to the descriptor until the residual error between the predicted and actual property values falls within predefined acceptable limits. The resulting descriptor is an analytical function that succinctly captures the relationship between the selected features and the EFA. This function serves as the basis for a predictive model that can be used to classify or predict properties of unseen materials.

In addition to SISSO, we also utilized random forest (RF), k-nearest neighbors (KNN), and support vector regression (SVR) algorithms to establish a benchmark for comparison. These established machine learning techniques were applied to the same dataset and underwent a k-fold cross-validation process, which is a widely accepted method for assessing the generalization performance of a model. The process involved partitioning the dataset into 'k' equally sized subsets (or folds), where each fold was used as a validation set while the remaining 'k-1' folds were used for training. This procedure was repeated 'k' times, with each fold serving as the validation set once, ensuring a robust evaluation of the model's predictive capabilities. Figure 1, which illustrates the k-fold cross-validation process, is provided to offer a visual representation of how the data were divided and utilized across the different folds. Ultimately, we chose to implement a 5-fold cross-validation for our models, as it struck a balance between thorough evaluation and computational efficiency, allowing for a direct comparison of predictive performance across different modeling approaches. To assess the performance of our models, we employed four statistical methods: (a) mean squared error (MSE), (b) mean absolute error (MAE), (c) root mean squared error (RMSE), and (d) R-squared (R^2). These metrics provided a comprehensive evaluation of the models' accuracy and reliability in making predictions.

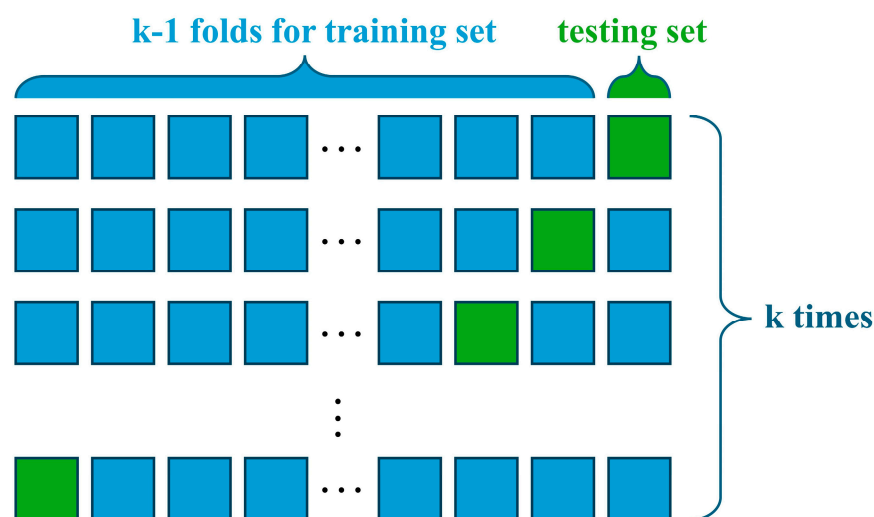


Figure 1. Schematic of the k-fold cross-validation.

The main parameters for these algorithms are detailed in Table 1. By employing this comparative analysis, we aimed to evaluate the effectiveness of SISSO in the context of HEN ceramics and to ensure that our models were not overfitting the training data, but were well-equipped to make accurate predictions on new, unseen materials, thereby enhancing

the reliability and applicability of our models. The flowchart for predicting the EFA of HEN ceramics using SISSO is shown in Figure 2.

Table 1. Main parameters for the machine learning models in this work.

Model	Tuning Parameters
KNN	n_neighbors = 3
SVR	Kernel = 'rbf', Gamma = 0.001, C = 100
RF	Random_state = 1050, Max_depth = 6, N_estimators = 100
SISSO	ops = '(+)(-)(*)(/)(exp)(exp-)', nf_sis = 20

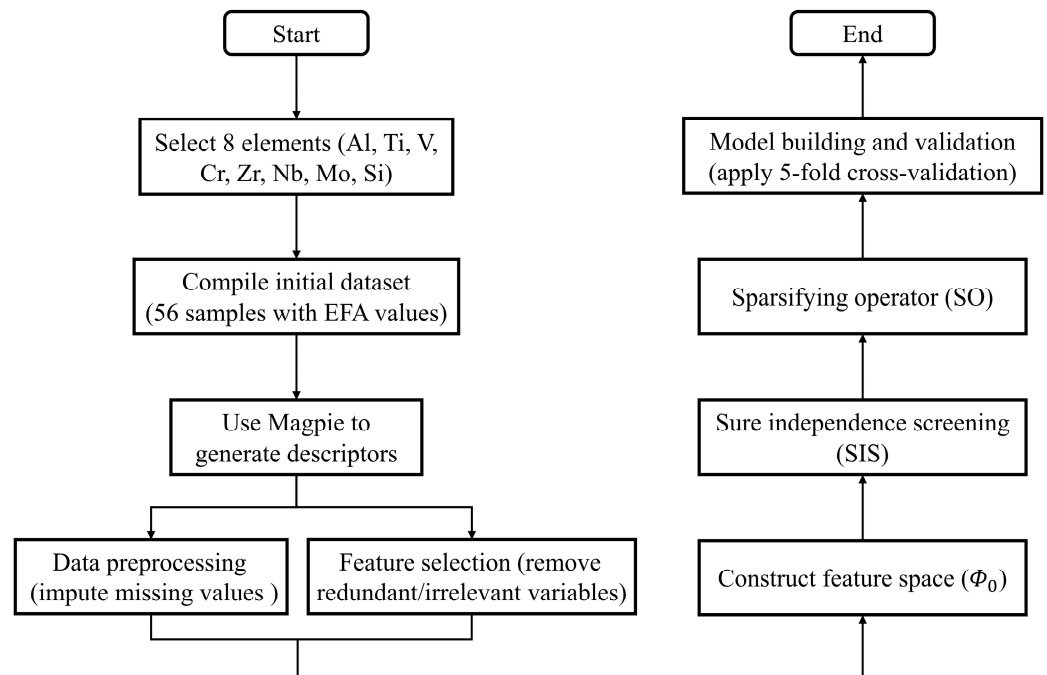


Figure 2. SISSO flowchart for EFA prediction in HEN ceramics.

3. Results and Discussion

3.1. Performance of SISSO Model for Predictions of EFA

Utilizing the 5-fold cross-validation approach, the SISSO model derived a function that best predicted the EFA values of HEN ceramics on testing set. The resulting function, which was a product of the SISSO model's feature selection and sparsification process, is as follows:

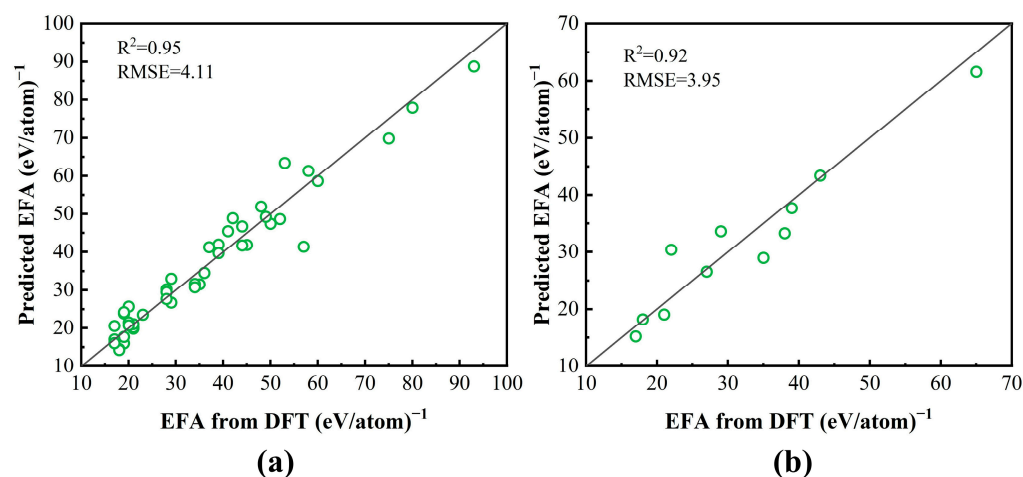
$$\text{EFA} = 27896.18 \times \left(\frac{\text{MMADNV}}{\frac{\text{MMGSV}}{\frac{\text{APVE}}{\text{AIC}}}} \right) - 0.90 \times \left(\frac{\text{ADVE} - \text{APVE}}{\text{MMN} - \text{MRGSV}} \right) - 63.15 \quad (4)$$

Table 2 provides a comprehensive explanation of the feature descriptors in Equation (4) that were identified by the SISSO model as being significant in predicting the EFA values. Each descriptor is detailed with its specific meaning. This equation serves as a quantitative tool that captures the complex relationships between the elemental composition and EFA values, providing a basis for predicting the stability of HEN ceramics.

The predictive performance of the SISSO model is evidenced in Figure 3a, where the model's predictions are compared with the actual EFA values obtained from DFT simulations for the training set, which consisted of 45 samples in each fold of the 5-fold cross-validation process. The data points are distributed around the diagonal line, which represents perfect prediction accuracy. The close proximity of the points to the line indicates that the SISSO model effectively captured the intrinsic relationships between the elemental compositions and their respective EFA values within the training dataset.

Table 2. The meaning of each feature descriptor in the function form obtained by SISO.

Feature Descriptors	Descriptions
MADNV	Average deviation of number of filled p orbitals
MMGSV	Maximum DFT-computed volume of elemental solid
APVE	Fraction-weighted average of the total valence electrons in the p orbital
AIC	The mean ionic character for the composition
ADVE	Fraction-weighted average of the total valence electrons in the d orbital
MMN	Mode atomic number
MRGSV	Range DFT-computed volume of elemental solid

**Figure 3.** Predictions of EFA for (a) the training set of 45 samples and (b) testing set of 11 samples using the SISO model against real values from DFT simulations in [32].

Building upon the performance demonstrated in the training set, Figure 3b evaluates the SISO model's predictive capabilities on the testing set with 11 samples, which comprised new, unseen compositions compared to the training set. Similar to the training set analysis, the model's predictions were plotted against the actual EFA values from DFT simulations. The scatter plot shows that the model maintained a high level of accuracy, with a slight increase in the scatter, reflected in the marginally lower R^2 value compared to the training set. This was an expected outcome, as the model was generalizing from the training data to new compositions. Nonetheless, the results confirmed the robustness of the SISO model in predicting EFA for HEN ceramics, even in the absence of prior data. The distribution of residuals for the training and testing sets, illustrated in Figure A1, provided further insight into the model's predictive accuracy. The uniform distribution of residuals indicated that the model's predictions were generally unbiased and reliable across the range of compositions evaluated.

Figure 4 provides a comparative analysis of the performance of the SISO model alongside other machine learning models, including KNN, SVR, and RF, on the training set. The figure is divided into four parts, each corresponding to a different performance metric: MSE, MAE, RMSE, and R^2 . Each bar chart represents the average performance of the models based on the 5-fold cross-validation process. The SISO model outperformed the others, with the shortest bars in the MSE, MAE, and RMSE charts, indicating lower prediction errors. The highest bars in the R^2 chart demonstrate SISO's superior ability to explain variance in the training data, suggesting a better fit and predictive accuracy. Figure 5 shows the performance of the same models on the testing set. The SISO model maintained its lead, with the lowest error bars and the highest R^2 values, confirming its robust generalization capabilities. The consistent outperformance of SISO across both datasets underscores its reliability and potential for practical application in materials science.

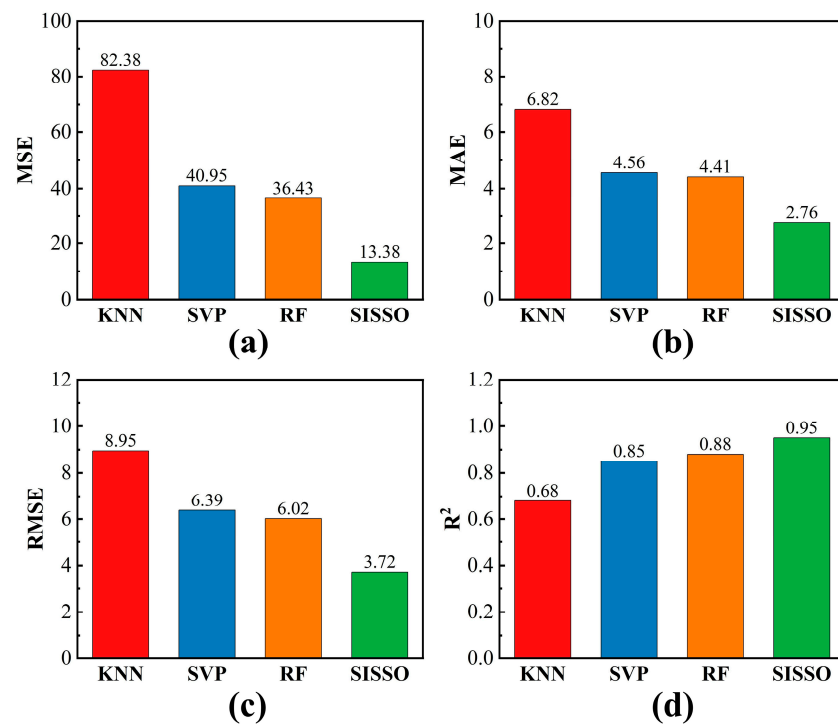


Figure 4. Comparison of (a) MSE, (b) MAE, (c) RMSE, and (d) R^2 across the four machine learning models on the training set. The red, blue, orange, and green bars represent the performance of KNN, SVP, RF, and SISSO, respectively.

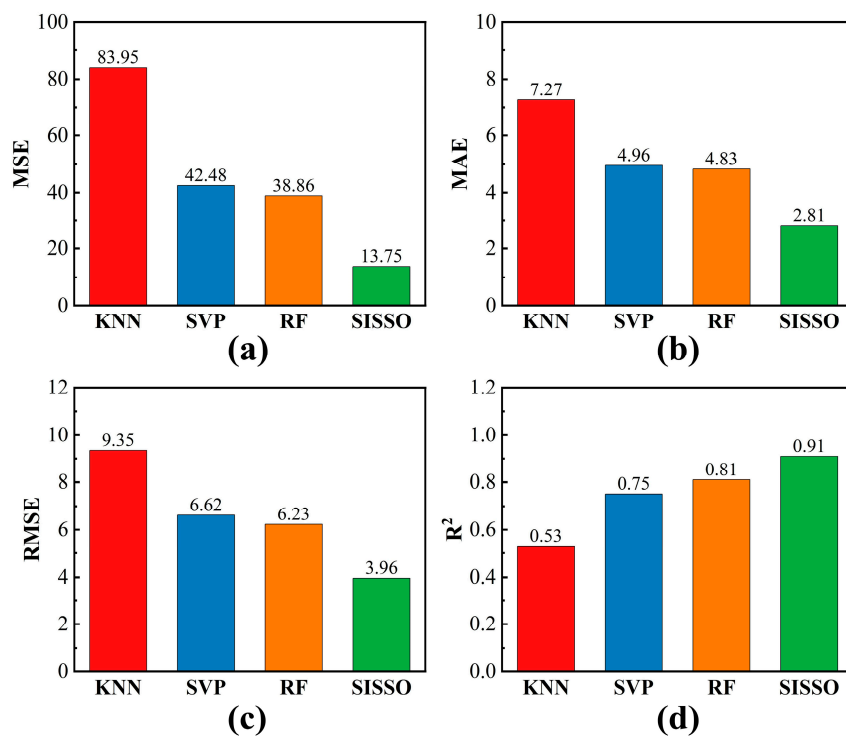


Figure 5. Comparison of (a) MSE, (b) MAE, (c) RMSE, and (d) R^2 across the four machine learning models on the testing set. The red, blue, orange, and green bars represent the performance of KNN, SVP, RF, and SISSO, respectively.

3.2. Applications of SISSO Model for New HEN Ceramics

The predictive capabilities of the SISSO model were extended to explore novel HEN ceramics by incorporating additional elements such as Hf, Ta, and W. The resultant 210 novel HENs had not been previously calculated using DFT. These predictions signified an extension of our model's utility in exploring new materials with potentially superior attributes. The model's predictions, as detailed in Table 3, revealed a range of new compositions with EFA values exceeding $60 \text{ (eV/atom)}^{-1}$, which indicated their potential to form stable single-phase structures. The more comprehensive data can be found in Table A2 of Appendix A. In the predicted new HEN ceramics, the systems AlTiCrNbTa₅N₅, TiVNbMoTa₅N₅, and AlVCrNbTa₅N₅ exhibited notably high EFA values of 93.52, 84.01, and 81.89 (eV/atom)^{-1} , respectively. These high EFA values suggested a strong propensity for these compounds to form stable single-phase structures, which is crucial for their potential as advanced materials with superior properties for high-performance applications.

Table 3. New HEN ceramics with EFA greater than 60 predicted by SISSO.

Formula	EFA (eV/atom)^{-1}	Formula	EFA (eV/atom)^{-1}
TiVCrZrHfN ₅	73.81	AlTiCrMoTa ₅ N ₅	66.19
TiVCrNbHfN ₅	72.37	AlTiNbMoTa ₅ N ₅	66.36
TiVCrMoHfN ₅	62.62	AlVCrNbTa ₅ N ₅	81.89
TiVZrNbHfN ₅	75.07	AlVCrMoTa ₅ N ₅	61.98
TiVZrMoHfN ₅	66.71	AlVNbMoTa ₅ N ₅	63.48
TiVNbMoHfN ₅	64.26	TiVCrZrTa ₅ N ₅	68.14
TiCrZrNbHfN ₅	74.49	TiVCrNbTa ₅ N ₅	76.59
TiCrZrMoHfN ₅	66.03	TiVCrMoTa ₅ N ₅	78.62
TiCrNbMoHfN ₅	63.48	TiVZrNbTa ₅ N ₅	69.48
TiZrNbMoHfN ₅	67.48	TiVZrMoTa ₅ N ₅	60.56
VCrZrNbHfN ₅	72.43	TiVNbMoTa ₅ N ₅	84.01
VCrZrMoHfN ₅	63.69	TiCrZrNbTa ₅ N ₅	68.86
VCrNbMoHfN ₅	60.89	TiZrNbMoTa ₅ N ₅	61.41
VZrNbMoHfN ₅	65.18	VCrZrNbTa ₅ N ₅	66.69
CrZrNbMoHfN ₅	64.47	AlTiVCrWN ₅	69.82
AlTiVCrTa ₅ N ₅	78.96	AlTiVNbWN ₅	60.90
AlTiVNbTa ₅ N ₅	76.47	AlTiCrNbWN ₅	68.83
AlTiVMoTa ₅ N ₅	65.95	TiVCrMoWN ₅	71.32
AlTiCrNbTa ₅ N ₅	93.52	TiVNbMoWN ₅	62.83

The SISSO model's predictive capabilities were further substantiated by the successful experimental synthesis of several compositions reported previously with high EFA values. Notably, the systems (TiVZrNbHf)_xN_x, (TiCrZrNbHf)_xN_x, (TiVCrNbTa)_xN_x, (AlTiVZrTa)_xN_x, and (AlTiCrZrTa)_xN_x, which were predicted by the SISSO model to have EFA values of 75.07, 74.49, 76.59, 52.55, and 52.06 (eV/atom)^{-1} , respectively, were realized in the experiment [39–45]. Some researchers experimentally suggest that Ti, Zr, Nb, and Ta elements have stronger nitride formation abilities. In line with this, our machine learning predictions for HEN ceramics containing these elements, such as TiVZrNbTa₅N₅ and TiCrZrNbTa₅N₅, also indicated high EFA values of up to 69.48 and 68.86 (eV/atom)^{-1} , respectively [46]. These experimental validations not only confirmed the model's accuracy but also showcased its potential for guiding the discovery of new HEN ceramics with promising properties. The successful synthesis of these materials opens up new avenues for exploring their potential applications in areas requiring materials with high thermal stability, excellent mechanical strength, and resistance to extreme environmental conditions.

It is worth noting that HEN ceramics with an EFA greater than 60 typically do not include Si, as observed in Table 3. Figure 6 provides a histogram intuitively comparing the distribution of predicted EFA values for new HEN ceramics with and without the inclusion of Si. The histogram reveals that the presence of Si tends to result in lower EFA values, which may be associated with the significant lattice distortion known to be induced by Si. Such distortion affects the material's propensity to form a stable single-phase structure, as

a uniform distribution of atoms is generally favored for higher EFA values. Our findings align with those of an existing study [32], which also reported that the incorporation of Si led to a compacting of the crystal lattice and consequently, a reduction in the EFA.

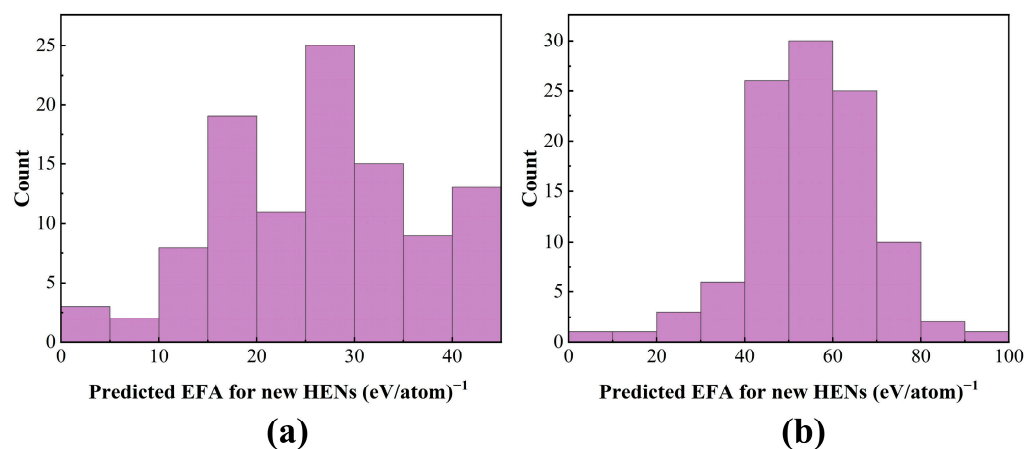


Figure 6. EFA distribution histogram of predicted 210 new high-entropy nitride ceramics (a) with Si (b) and without Si.

4. Conclusions

This study represents a significant advance in the application of machine learning techniques for the prediction of EFA in HENs. The SISSO model, with its “white-box” interpretability, was successfully applied to predict EFA values, offering a deeper understanding of the factors that contribute to the formation and stability of single-phase HENs. The model’s predictions were validated against theoretical benchmarks, showcasing its effectiveness as a predictive tool in materials science. This not only enhances the accuracy of EFA prediction but also provides a transparent framework for interpreting the complex interactions between elemental composition and material properties.

In the predicted new HEN ceramics, the study identified several systems with notably high EFA values, indicating their potential to form stable single-phase structures. Specifically, the systems AlTiCrNbTaN₅, TiVNbMoTa₅N₅, and AlVCrNbTa₅N₅ stood out with EFA values of 93.52, 84.01, and 81.89 (eV/atom)⁻¹, respectively. These high EFA values are indicative of the strong propensity of these compounds to form stable single-phase structures, which is crucial to their potential as advanced materials with superior properties for high-performance applications. The identification of these compositions through the SISSO model not only demonstrates the predictive power of the model but also highlights the potential of these specific HEN systems in further research and development. This discovery underscores the capability of the SISSO model to guide experimental efforts towards the synthesis of new materials with tailored properties, expediting the process of material innovation and advancement.

Furthermore, the successful experimental synthesis of several compositions predicted by the SISSO model with high EFA values confirmed the model’s accuracy and its potential for guiding the discovery of new HEN ceramics with promising properties. This research underscores the transformative impact of data-driven approaches in materials science, paving the way for the accelerated development of next-generation materials with superior performance characteristics. The ability to predict and validate the EFA of new materials will likely revolutionize the field, enabling the design of materials that can withstand extreme conditions and perform beyond the capabilities of current materials. Additionally, while this work has mainly focused on the bulk phase materials of HEN ceramics, thin films of HEN ceramics are also worthy of study due to their significant applications. For the EFA prediction of HEN ceramic thin films, to ensure accuracy, EFA values related to thin films are also required. The structural features and polymorphic transformations of nitride ceramics were not incorporated into our model. We will expand on these in our future

research. This study is a testament to the power of combining computational modeling with experimental validation, forging a path for the rapid advancement of materials science in the era of data-driven research.

Author Contributions: Conceptualization, T.L. and R.W.; methodology, T.L.; software, T.L.; validation, T.L., R.W. and D.L.; formal analysis, T.L.; investigation, T.L. and R.W.; resources, D.L.; data curation, T.L.; writing—original draft preparation, T.L.; writing—review and editing, T.L., R.W. and D.L.; visualization, T.L.; supervision, D.L.; project administration, R.W.; funding acquisition, D.L. All authors have read and agreed to the published version of the manuscript.

Funding: This research received no external funding.

Data Availability Statement: The raw data supporting the conclusions of this article will be made available by the authors on request.

Conflicts of Interest: The authors declare no conflicts of interest.

Appendix A

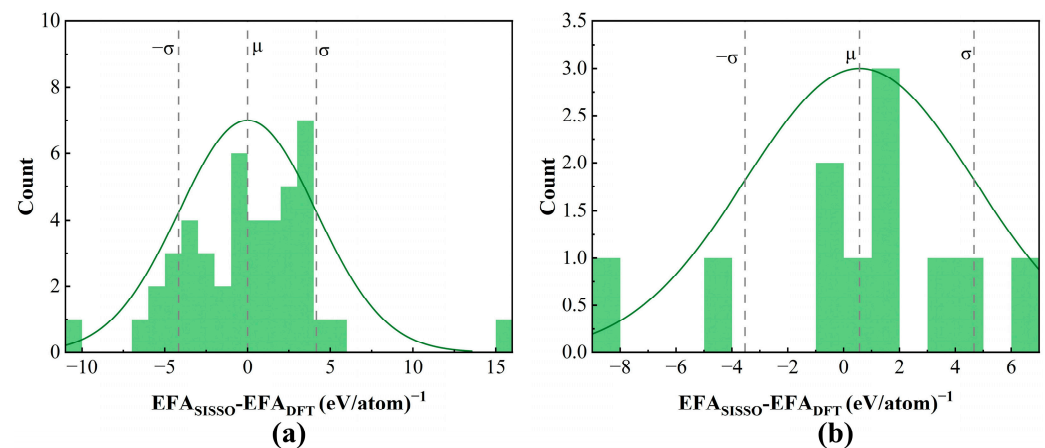


Figure A1. Distribution of residuals between the SISSO-learned descriptor and DFT simulations on the (a) training set and (b) testing set. The green curves represent the fitted normal distribution curves.

Table A1. EFA values from DFT simulations in [32].

Formula	EFA (eV/atom) ⁻¹
AlCrNbTiVN ₅	93
CrNbTiVZrN ₅	80
AlCrMoTiVN ₅	75
AlMoNbTiVN ₅	65
MoNbTiVZrN ₅	60
AlCrMoNbTiN ₅	58
AlCrMoTiZrN ₅	57
CrMoTiVZrN ₅	53
AlNbTiVZrN ₅	52
AlCrNbVZrN ₅	50
AlCrMoNbVN ₅	49
CrMoNbTiZrN ₅	48
AlMoNbVZrN ₅	45
CrMoNbTiVN ₅	44
AlCrTiVZrN ₅	44
AlMoNbTiZrN ₅	43
AlCrNbTiZrN ₅	42
CrMoNbVZrN ₅	41

Table A1. Cont.

Formula	EFA (eV/atom) ⁻¹
AlCrMoNbZrN ₅	39
AlCrMoVZrN ₅	39
CrNbSiTiVN ₅	39
NbSiTiVZrN ₅	38
AlMoTiVZrN ₅	37
CrNbSiTiZrN ₅	36
CrMoSiTiVN ₅	35
CrMoNbSiVN ₅	35
MoNbSiTiVN ₅	34
CrSiTiVZrN ₅	34
CrNbSiVZrN ₅	29
MoSiTiVZrN ₅	29
CrMoNbSiTiN ₅	29
MoNbSiTiZrN ₅	28
MoNbSiVZrN ₅	28
CrMoSiTiZrN ₅	28
CrMoSiVZrN ₅	27
AlCrSiTiVN ₅	23
CrMoNbSiZrN ₅	22
AlSiTiVZrN ₅	21
AlCrSiTiZrN ₅	21
AlCrSiVZrN ₅	21
AlCrNbSiZrN ₅	21
AlNbSiTiZrN ₅	20
AlCrNbSiTiN ₅	20
AlNbSiVZrN ₅	20
AlNbSiTiVN ₅	19
AlCrMoSiVN ₅	19
AlCrMoSiTiN ₅	19
AlCrNbSiVN ₅	19
AlCrMoSiZrN ₅	18
AlMoSiVZrN ₅	18
AlCrMoNbSiN ₅	18
AlMoSiTiVN ₅	17
AlMoSiTiZrN ₅	17
AlMoNbSiVN ₅	17
AlMoNbSiZrN ₅	17
AlMoNbSiTiN ₅	17

Table A2. The EFA of new HEN ceramics predicted by SISSO.

Formula	EFA (eV/atom) ⁻¹	Formula	EFA (eV/atom) ⁻¹	Formula	EFA (eV/atom) ⁻¹
AlSiTiVHfN ₅	26.22	AlSiTiVTaN ₅	27.40	AlSiTiVWN ₅	15.62
AlSiTiCrHfN ₅	25.95	AlSiTiCrTa ₅	28.58	AlSiTiCrWN ₅	16.52
AlSiTiZrHfN ₅	27.83	AlSiTiZrTa ₅	23.81	AlSiTiZrWN ₅	14.18
AlSiTiNbHfN ₅	25.13	AlSiTiNbTa ₅	30.73	AlSiTiNbWN ₅	18.78
AlSiTiMoHfN ₅	18.08	AlSiTiMoTa ₅	22.35	AlSiTiMoWN ₅	8.29
AlSiVCrHfN ₅	24.25	AlSiVCrTa ₅	26.67	AlSiVCrWN ₅	14.30
AlSiVZrHfN ₅	26.76	AlSiVZrTa ₅	22.63	AlSiVZrWN ₅	12.69
AlSiVNbHfN ₅	25.15	AlSiVNbTa ₅	26.52	AlSiVNbWN ₅	14.53
AlSiVMoHfN ₅	17.74	AlSiVMoTa ₅	18.20	AlSiVMoWN ₅	4.09
AlSiCrZrHfN ₅	26.42	AlSiCrZrTa ₅	22.27	AlSiCrZrWN ₅	12.21
AlSiCrNbHfN ₅	24.83	AlSiCrNbTa ₅	27.35	AlSiCrNbWN ₅	15.08
AlSiCrMoHfN ₅	17.33	AlSiCrMoTa ₅	18.78	AlSiCrMoWN ₅	4.40
AlSiZrNbHfN ₅	26.93	AlSiZrNbTa ₅	22.86	AlSiZrNbWN ₅	13.05
AlSiZrMoHfN ₅	20.46	AlSiZrMoTa ₅	16.01	AlSiZrMoWN ₅	4.33
AlSiNbMoHfN ₅	17.22	AlSiNbMoTa ₅	20.77	AlSiNbMoWN ₅	6.50

Table A2. Cont.

Formula	EFA (eV/atom) ⁻¹	Formula	EFA (eV/atom) ⁻¹	Formula	EFA (eV/atom) ⁻¹
AlTiVCrHfN ₅	55.10	AlTiVCrTa ₅ N ₅	78.96	AlTiVCrWN ₅	69.82
AlTiVZrHfN ₅	57.45	AlTiVZrTa ₅ N ₅	52.55	AlTiVZrWN ₅	41.40
AlTiVNbHfN ₅	56.26	AlTiVNbTa ₅ N ₅	76.47	AlTiVNbWN ₅	60.90
AlTiVMoHfN ₅	47.89	AlTiVMoTa ₅ N ₅	65.95	AlTiVMoWN ₅	56.72
AlTiCrZrHfN ₅	57.00	AlTiCrZrTa ₅ N ₅	52.06	AlTiCrZrWN ₅	40.78
AlTiCrNbHfN ₅	55.78	AlTiCrNbTa ₅ N ₅	93.52	AlTiCrNbWN ₅	68.83
AlTiCrMoHfN ₅	47.30	AlTiCrMoTa ₅ N ₅	66.19	AlTiCrMoWN ₅	55.51
AlTiZrNbHfN ₅	57.84	AlTiZrNbTa ₅ N ₅	53.00	AlTiZrNbWN ₅	42.01
AlTiZrMoHfN ₅	50.62	AlTiZrMoTa ₅ N ₅	45.30	AlTiZrMoWN ₅	31.94
AlTiNbMoHfN ₅	48.16	AlTiNbMoTa ₅ N ₅	66.36	AlTiNbMoWN ₅	47.95
AlVCrZrHfN ₅	55.20	AlVCrZrTa ₅ N ₅	50.16	AlVCrZrWN ₅	38.53
AlVCrNbHfN ₅	53.76	AlVCrNbTa ₅ N ₅	81.89	AlVCrNbWN ₅	56.74
AlVCrMoHfN ₅	45.03	AlVCrMoTa ₅ N ₅	61.98	AlVCrMoWN ₅	53.25
AlVZrNbHfN ₅	56.28	AlVZrNbTa ₅ N ₅	51.32	AlVZrNbWN ₅	39.94
AlVZrMoHfN ₅	48.78	AlVZrMoTa ₅ N ₅	43.33	AlVZrMoWN ₅	29.58
AlVNbMoHfN ₅	46.44	AlVNbMoTa ₅ N ₅	63.48	AlVNbMoWN ₅	44.59
AlCrZrNbHfN ₅	55.80	AlCrZrNbTa ₅ N ₅	50.80	AlCrZrNbWN ₅	39.29
AlCrZrMoHfN ₅	48.21	AlCrZrMoTa ₅ N ₅	42.73	AlCrZrMoWN ₅	28.84
AlCrNbMoHfN ₅	45.80	AlCrNbMoTa ₅ N ₅	53.49	AlCrNbMoWN ₅	25.47
AlZrNbMoHfN ₅	49.37	AlZrNbMoTa ₅ N ₅	43.99	AlZrNbMoWN ₅	30.39
SiTiVCrHfN ₅	40.02	SiTiVCrTa ₅ N ₅	43.11	SiTiVCrWN ₅	29.01
SiTiVZrHfN ₅	42.79	SiTiVZrTa ₅ N ₅	38.06	SiTiVZrWN ₅	26.76
SiTiVNbHfN ₅	41.13	SiTiVNbTa ₅ N ₅	43.64	SiTiVNbWN ₅	29.97
SiTiVMoHfN ₅	32.70	SiTiVMoTa ₅ N ₅	34.14	SiTiVMoWN ₅	18.01
SiTiCrZrHfN ₅	42.36	SiTiCrZrTa ₅ N ₅	37.59	SiTiCrZrWN ₅	26.17
SiTiCrNbHfN ₅	40.68	SiTiCrNbTa ₅ N ₅	43.87	SiTiCrNbWN ₅	29.90
SiTiCrMoHfN ₅	32.14	SiTiCrMoTa ₅ N ₅	34.12	SiTiCrMoWN ₅	17.69
SiTiZrNbHfN ₅	43.13	SiTiZrNbTa ₅ N ₅	38.47	SiTiZrNbWN ₅	27.31
SiTiZrMoHfN ₅	35.78	SiTiZrMoTa ₅ N ₅	30.68	SiTiZrMoWN ₅	17.35
SiTiNbMoHfN ₅	32.77	SiTiNbMoTa ₅ N ₅	35.98	SiTiNbMoWN ₅	19.70
SiVCrZrHfN ₅	40.59	SiVCrZrTa ₅ N ₅	35.73	SiVCrZrWN ₅	23.99
SiVCrNbHfN ₅	38.71	SiVCrNbTa ₅ N ₅	41.65	SiVCrNbWN ₅	27.32
SiVCrMoHfN ₅	29.94	SiVCrMoTa ₅ N ₅	31.65	SiVCrMoWN ₅	14.85
SiVZrNbHfN ₅	41.64	SiVZrNbTa ₅ N ₅	36.86	SiVZrNbWN ₅	25.34
SiVZrMoHfN ₅	34.03	SiVZrMoTa ₅ N ₅	28.81	SiVZrMoWN ₅	15.12
SiVNbMoHfN ₅	31.29	SiVNbMoTa ₅ N ₅	32.88	SiVNbMoWN ₅	16.50
SiCrZrNbHfN ₅	41.18	SiCrZrNbTa ₅ N ₅	36.36	SiCrZrNbWN ₅	24.72
SiCrZrMoHfN ₅	33.49	SiCrZrMoTa ₅ N ₅	28.23	SiCrZrMoWN ₅	14.42
SiCrNbMoHfN ₅	30.69	SiCrNbMoTa ₅ N ₅	32.51	SiCrNbMoWN ₅	15.84
SiZrNbMoHfN ₅	34.57	SiZrNbMoTa ₅ N ₅	29.41	SiZrNbMoWN ₅	15.87
TiVCrZrHfN ₅	73.81	TiVCrZrTa ₅ N ₅	68.14	TiVCrZrWN ₅	55.16
TiVCrNbHfN ₅	72.37	TiVCrNbTa ₅ N ₅	76.59	TiVCrNbWN ₅	49.54
TiVCrMoHfN ₅	62.62	TiVCrMoTa ₅ N ₅	78.62	TiVCrMoWN ₅	71.32
TiVZrNbHfN ₅	75.07	TiVZrNbTa ₅ N ₅	69.48	TiVZrNbWN ₅	56.78
TiVZrMoHfN ₅	66.71	TiVZrMoTa ₅ N ₅	60.56	TiVZrMoWN ₅	45.16
TiVNbMoHfN ₅	64.26	TiVNbMoTa ₅ N ₅	84.01	TiVNbMoWN ₅	62.83
TiCrZrNbHfN ₅	74.49	TiCrZrNbTa ₅ N ₅	68.86	TiCrZrNbWN ₅	56.01
TiCrZrMoHfN ₅	66.03	TiCrZrMoTa ₅ N ₅	59.84	TiCrZrMoWN ₅	44.29
TiCrNbMoHfN ₅	63.48	TiCrNbMoTa ₅ N ₅	46.97	TiCrNbMoWN ₅	16.64
TiZrNbMoHfN ₅	67.48	TiZrNbMoTa ₅ N ₅	61.41	TiZrNbMoWN ₅	46.18
VCrZrNbHfN ₅	72.43	VCrZrNbTa ₅ N ₅	66.69	VCrZrNbWN ₅	53.44
VCrZrMoHfN ₅	63.69	VCrZrMoTa ₅ N ₅	57.39	VCrZrMoWN ₅	41.43
VCrNbMoHfN ₅	60.89	VCrNbMoTa ₅ N ₅	34.62	VCrNbMoWN ₅	3.77
VZrNbMoHfN ₅	65.18	VZrNbMoTa ₅ N ₅	58.97	VZrNbMoWN ₅	43.30
CrZrNbMoHfN ₅	64.47	CrZrNbMoTa ₅ N ₅	58.21	CrZrNbMoWN ₅	42.39

References

- Schweidler, S.; Botros, M.; Strauss, F.; Wang, Q.S.; Ma, Y.J.; Velasco, L.; Marques, G.C.; Sarkar, A.; Kübel, C.; Hahn, H.; et al. High-entropy materials for energy and electronic applications. *Nat. Rev. Mater.* **2024**, *9*, 266–281. [[CrossRef](#)]
- Deng, C.; Wang, T.; Wu, P.W.; Zhu, W.S.; Dai, S. High entropy materials for catalysis: A critical review of fundamental concepts and applications. *Nano Energy* **2024**, *120*, 109153. [[CrossRef](#)]
- Wang, Q.S.; Velasco, L.; Breitung, B.; Presser, V. High-Entropy Energy Materials in the Age of Big Data: A Critical Guide to Next-Generation Synthesis and Applications. *Adv. Energy Mater.* **2021**, *11*, 2102355. [[CrossRef](#)]
- Sun, Y.F.; Dai, S. High-entropy materials for catalysis: A new frontier. *Sci. Adv.* **2021**, *7*, eabg1600. [[CrossRef](#)] [[PubMed](#)]
- Zu, Y.F.; Wang, Z.; Tian, H.L.; Wu, F.; Fu, L.S.; Dai, J.X.; Sha, J.J. A Novel Preparation Method of (Ti,Zr,Nb,Mo,W)B-SiC Composite Ceramic Based on Reactive Sintering of Pre-Alloyed Metals. *Crystals* **2024**, *14*, 14. [[CrossRef](#)]
- Alleg, S.; Bekhouche, A.; Hachache, H.; Sunol, J.J. Effect of Aluminum Addition on the Microstructure, Magnetic, and Mechanical Properties of FeCrCoNiMn High-Entropy Alloy. *Crystals* **2023**, *13*, 1483. [[CrossRef](#)]
- Zhang, Y.; Zuo, T.T.; Tang, Z.; Gao, M.C.; Dahmen, K.A.; Liaw, P.K.; Lu, Z.P. Microstructures and properties of high-entropy alloys. *Prog. Mater. Sci.* **2014**, *61*, 1–93. [[CrossRef](#)]
- Anamu, U.S.; Ayodele, O.O.; Olorundaisi, E.; Babalola, B.J.; Odetola, P.I.; Ogunmefun, A.; Ukoba, K.; Jen, T.C.; Olubambi, P.A. Fundamental design strategies for advancing the development of high entropy alloys for thermo-mechanical application: A critical review. *J. Mater. Res. Technol.* **2023**, *27*, 4833–4860. [[CrossRef](#)]
- Liu, Y.F.; Ren, J.; Liu, J.; Cao, Y.; Liu, W.; Li, T.Y.; Zhu, Y.T.; Chen, W. Exceptional thermal stability of additively manufactured CoCrFeMnNi high-entropy alloy with cellular dislocation structures. *Mater. Sci. Eng. A Struct.* **2023**, *885*, 145650. [[CrossRef](#)]
- Yan, W.Q.; Zhao, Y.M.; Zhang, Y.F.; Li, Q.; Chen, S.N.; Yuan, H.; Zhang, Z.Q.; Chen, L.; Luo, J.; Pang, P.; et al. Corrosion-resistant and interfacial conductive AlTiVCrMo high-entropy alloy and (AlTiVCrMo)_{Nx} high-entropy ceramics coatings for surface modification of bipolar plates in proton exchange membrane fuel cells. *J. Power Sources* **2022**, *527*, 231217. [[CrossRef](#)]
- Zhang, P.; Liu, X.J.; Cai, A.H.; Du, Q.; Yuan, X.Y.; Wang, H.; Wu, Y.; Jiang, S.H.; Lu, Z.P. High-entropy carbide-nitrides with enhanced toughness and sinterability. *Sci. China Mater.* **2021**, *64*, 2037–2044. [[CrossRef](#)]
- Moskovskikh, D.; Vorotilo, S.; Buinevich, V.; Sedegov, A.; Kuskov, K.; Khort, A.; Shuck, C.; Zhukovskiy, M.; Mukasyan, A. Extremely hard and tough high entropy nitride ceramics. *Sci. Rep.* **2020**, *10*, 19874. [[CrossRef](#)] [[PubMed](#)]
- Sarker, P.; Harrington, T.; Toher, C.; Oses, C.; Samiee, M.; Maria, J.P.; Brenner, D.W.; Vecchio, K.S.; Curtarolo, S. High-entropy high-hardness metal carbides discovered by entropy descriptors. *Nat. Commun.* **2018**, *9*, 4980. [[CrossRef](#)] [[PubMed](#)]
- Harrington, T.J.; Gild, J.; Sarker, P.; Toher, C.; Rost, C.M.; Dippo, O.F.; McElfresh, C.; Kaufmann, K.; Marin, E.; Borowski, L.; et al. Phase stability and mechanical properties of novel high entropy transition metal carbides. *Acta Mater.* **2019**, *166*, 271–280. [[CrossRef](#)]
- Divilov, S.; Eckert, H.; Hicks, D.; Oses, C.; Toher, C.; Friedrich, R.; Esters, M.; Mehl, M.J.; Zettel, A.C.; Lederer, Y.; et al. Disordered enthalpy–entropy descriptor for high-entropy ceramics discovery. *Nature* **2024**, *625*, 66–73. [[CrossRef](#)] [[PubMed](#)]
- Zhang, J.; Xu, B.A.; Xiong, Y.X.; Ma, S.H.; Wang, Z.; Wu, Z.G.; Zhao, S.J. Design high-entropy carbide ceramics from machine learning. *Npj Comput. Mater.* **2022**, *8*, 5. [[CrossRef](#)]
- Kaufmann, K.; Maryanovsky, D.; Mellor, W.M.; Zhu, C.Y.; Rosengarten, A.S.; Harrington, T.J.; Oses, C.; Toher, C.; Curtarolo, S.; Vecchio, K.S. Discovery of high-entropy ceramics via machine learning. *Npj Comput. Mater.* **2020**, *6*, 42. [[CrossRef](#)]
- Dong, H.Q.; Tao, X.M.; Paulasto-Kröckel, M. Calculation of Phase Diagrams and First-Principles Study of Germanium Impacts on Phosphorus Distribution in Czochralski Silicon. *J. Electron. Mater.* **2021**, *50*, 4272–4288. [[CrossRef](#)]
- Chen, Q.; Yang, C.; Xing, T.; Xi, J.; Zhang, W.; Yang, J.; Xi, L. Defect engineering and alloying strategies for tailoring thermoelectric behavior in GeTe and its alloys. *J. Mater.* **2024**. [[CrossRef](#)]
- Emery, A.A.; Wolverton, C. High-throughput DFT calculations of formation energy, stability and oxygen vacancy formation energy of ABO₃ perovskites. *Sci. Data* **2017**, *4*, 170153. [[CrossRef](#)]
- Wu, Y.L.; Wang, C.F.; Ju, M.G.; Jia, Q.Q.; Zhou, Q.H.; Lu, S.H.; Gao, X.Y.; Zhang, Y.; Wang, J.L. Universal machine learning aided synthesis approach of two-dimensional perovskites in a typical laboratory. *Nat. Commun.* **2024**, *15*, 138. [[CrossRef](#)] [[PubMed](#)]
- Jha, D.; Gupta, V.; Ward, L.; Yang, Z.J.; Wolverton, C.; Foster, I.; Liao, W.K.; Choudhary, A.; Agrawal, A. Enabling deeper learning on big data for materials informatics applications. *Sci. Rep.* **2021**, *11*, 4244. [[CrossRef](#)] [[PubMed](#)]
- Chong, S.S.; Ng, Y.S.; Wang, H.Q.; Zheng, J.C. Advances of machine learning in materials science: Ideas and techniques. *Front. Phys.* **2024**, *19*, 13501. [[CrossRef](#)]
- Pilania, G. Machine learning in materials science: From explainable predictions to autonomous design. *Comput. Mater. Sci.* **2021**, *193*, 110360. [[CrossRef](#)]
- Giles, S.A.; Sengupta, D.; Broderick, S.R.; Rajan, K. Machine-learning-based intelligent framework for discovering refractory high-entropy alloys with improved high-temperature yield strength. *Npj Comput. Mater.* **2022**, *8*, 235. [[CrossRef](#)]
- Peivaste, L.; Jossou, E.; Tiamiyu, A.A. Data-driven analysis and prediction of stable phases for high-entropy alloy design. *Sci. Rep.* **2023**, *13*, 22556. [[CrossRef](#)] [[PubMed](#)]
- Zhao, S.J. Application of machine learning in understanding the irradiation damage mechanism of high-entropy materials. *J. Nucl. Mater.* **2022**, *559*, 153462. [[CrossRef](#)]
- Schlenz, H.; Baumann, S.; Meulenber, W.A.; Guillon, O. The Development of New Perovskite-Type Oxygen Transport Membranes Using Machine Learning. *Crystals* **2022**, *12*, 947. [[CrossRef](#)]

29. Ouyang, R.H.; Curtarolo, S.; Ahmetcik, E.; Scheffler, M.; Ghiringhelli, L.M. SISSO: A compressed-sensing method for identifying the best low-dimensional descriptor in an immensity of offered candidates. *Phys. Rev. Mater.* **2018**, *2*, 083802. [[CrossRef](#)]
30. Schmidt, M.; Lipson, H. Distilling Free-Form Natural Laws from Experimental Data. *Science* **2009**, *324*, 81–85. [[CrossRef](#)]
31. Bartel, C.J.; Sutton, C.; Goldsmith, B.R.; Ouyang, R.H.; Musgrave, C.B.; Ghiringhelli, L.M.; Scheffler, M. New tolerance factor to predict the stability of perovskite oxides and halides. *Sci. Adv.* **2019**, *5*, eaav0693. [[CrossRef](#)] [[PubMed](#)]
32. Huang, H.Y.; Shao, L.H.; Liu, H.Z. Prediction of Single-Phase High-Entropy Nitrides from First-Principles Calculations. *Phys. Status Solidi B* **2021**, *258*, 2100140. [[CrossRef](#)]
33. Liu, Y.F.; Cui, X.F.; Jin, G.; Wen, X.; Wang, S.; Zhang, Y.P. In-situ array TiN reinforced Al-Cr-Ti-Nb-Mo refractory high-entropy alloy coating on Ti-6Al-4V alloy by gas assisted laser nitriding. *J. Alloys Compd.* **2024**, *981*, 173743. [[CrossRef](#)]
34. Lewin, E. Multi-component and high-entropy nitride coatings-A promising field in need of a novel approach. *J. Appl. Phys.* **2020**, *127*, 160901. [[CrossRef](#)]
35. Xing, Q.W.; Xia, S.Q.; Yan, X.H.; Zhang, Y. Mechanical properties and thermal stability of (NbTiAlSiZr)N high-entropy ceramic films at high temperatures. *J. Mater. Res.* **2018**, *33*, 3347–3354. [[CrossRef](#)]
36. Ward, L.; Agrawal, A.; Choudhary, A.; Wolverton, C. A general-purpose machine learning framework for predicting properties of inorganic materials. *Npj Comput. Mater.* **2016**, *2*, 16028. [[CrossRef](#)]
37. Ward, L.; Dunn, A.; Faghaninia, A.; Zimmermann, N.E.R.; Bajaj, S.; Wang, Q.; Montoya, J.; Chen, J.M.; Bystrom, K.; Dylla, M.; et al. Matminer: An open source toolkit for materials data mining. *Comput. Mater. Sci.* **2018**, *152*, 60–69. [[CrossRef](#)]
38. Wei, A.R.; Ye, H.; Guo, Z.L.; Xiong, J. SISSO-assisted prediction and design of mechanical properties of porous graphene with a uniform nanopore array. *Nanoscale Adv.* **2022**, *4*, 1455–1463. [[CrossRef](#)] [[PubMed](#)]
39. Dippo, O.F.; Mesgarzadeh, N.; Harrington, T.J.; Schrader, G.D.; Vecchio, K.S. Bulk high-entropy nitrides and carbonitrides. *Sci. Rep.* **2020**, *10*, 21288. [[CrossRef](#)]
40. Firstov, S.A.; Gorban', V.F.; Danilenko, N.I.; Karpets, M.V.; Andreev, A.A.; Makarenko, E.S. Thermal Stability of Superhard Nitride Coatings from High-Entropy Multicomponent Ti-V-Zr-Nb-Hf Alloy. *Powder Metall. Met. Ceram.* **2014**, *52*, 560–566. [[CrossRef](#)]
41. Hahn, R.; Kirnbauer, A.; Bartosik, M.; Kolozsvári, S.; Mayrhofer, P.H. Toughness of Si alloyed high-entropy nitride coatings. *Mater. Lett.* **2019**, *251*, 238–240. [[CrossRef](#)]
42. Lai, C.H.; Tsai, M.H.; Lin, S.J.; Yeh, J.W. Influence of substrate temperature on structure and mechanical, properties of multi-element (AlCrTaTiZr)N coatings. *Surf. Coat. Technol.* **2007**, *201*, 6993–6998. [[CrossRef](#)]
43. Sobol, O.V.; Andreev, A.A.; Gorban, V.F.; Postelnyk, H.O.; Stolbovoy, V.A.; Zvyagolsky, A.V.; Dolomanov, A.V.; Kraievskaya, Z.V. The Use of Negative Bias Potential for Structural Engineering of Vacuum-Arc Nitride Coatings Based on High-Entropy Alloys. *Probl. At. Sci. Technol.* **2019**, *120*, 127–135. [[CrossRef](#)]
44. Johansson, K.; Riekehr, L.; Fritze, S.; Lewin, E. Multicomponent Hf-Nb-Ti-V-Zr nitride coatings by reactive magnetron sputter deposition. *Surf. Coat. Technol.* **2018**, *349*, 529–539. [[CrossRef](#)]
45. Lai, C.H.; Lin, S.J.; Yeh, J.W.; Chang, S.Y. Preparation and characterization of AlCrTaTiZr multi-element nitride coatings. *Surf. Coat. Technol.* **2006**, *201*, 3275–3280. [[CrossRef](#)]
46. Wang, J.; Shu, R.; Chai, J.L.; Rao, S.G.; le Febvrier, A.; Wu, H.C.; Zhu, Y.B.; Yao, C.F.; Luo, L.H.; Li, W.P.; et al. Xe-ion-irradiation-induced structural transitions and elemental diffusion in high-entropy alloy and nitride thin-film multilayers. *Mater. Des.* **2022**, *219*, 110749. [[CrossRef](#)]

Disclaimer/Publisher's Note: The statements, opinions and data contained in all publications are solely those of the individual author(s) and contributor(s) and not of MDPI and/or the editor(s). MDPI and/or the editor(s) disclaim responsibility for any injury to people or property resulting from any ideas, methods, instructions or products referred to in the content.